MDPI

Article

Evaluating the Prediction Performance of the WRF-CUACE Model in Xinjiang, China

Yisilamu Wulayin [1,2,3,4,5], Huoqing Li [1,2,3,4,5], Lei Zhang [1,6], Ali Mamtimin [1,2,3,4,5], Junjian Liu [1,2,3,4,5], Wen Huo [1,2,3,4,*] and Hongli Liu [6]

1   Institute of Desert and Meteorology, China Meteorological Administration, Ürümqi 830002, China;
    yislm@idm.cn (Y.W.); lihq@idm.cn (H.L.); leiz09@cma.gov.cn (L.Z.); ali@idm.cn (A.M.); liujj@idm.cn (J.L.)
2   National Observation and Research Station of Desert Meteorology, Taklimakan Desert of Xinjiang,
    Ürümqi 830002, China
3   Taklimakan Desert Meteorology Field Experiment Station of CMA, Ürümqi 830002, China
4   Xinjiang Key Laboratory of Desert Meteorology and Sandstorm, Ürümqi 830002, China
5   Dabancheng National Special Test Feild for Comprehensive Meteorological Observation,
    Ürümqi 830002, China
6   Chinese Academy of Meteorological Science, Beijing 100081, China; liuhl@cma.gov.cn
*   Correspondence: huowenpet@idm.cn

Abstract: Dust and air pollution events are increasingly occurring around the Taklimakan Desert in southern Xinjiang and in the urban areas of northern Xinjiang. Predicting such events is crucial for the advancement, growth, and prosperity of communities. This study evaluated a dust and air pollution forecasting system based on the Weather Research and Forecasting model coupled with the China Meteorological Administration Chemistry Environment (WRF-CUACE) model using ground and satellite observations. The results showed that the forecasting system accurately predicted the formation, development, and termination of dust events. It demonstrated good capability for predicting the evolution and spatial distribution of dust storms, although it overestimated dust intensity. Specifically, the correlation coefficient (R) between simulated and observed PM10 was up to 0.85 with a mean absolute error (MAE) of 721.36 $\mu g \cdot m^{-3}$ during dust storm periods. During air pollution events, the forecasting system displayed notable variations in predictive accuracy across various urban areas. The simulated trends of PM2.5 and the Air Quality Index (AQI) closely aligned with the actual observations in Ürümqi. The R for simulated and observed PM2.5 concentrations at 24 and 48 h intervals were 0.60 and 0.54, respectively, with MAEs of 28.92 $\mu g \cdot m^{-3}$ and 29.10 $\mu g \cdot m^{-3}$, respectively. The correlation coefficients for simulated and observed AQIs at 24 and 48 h intervals were 0.79 and 0.70, respectively, with MAEs of 24.21 and 27.56, respectively. The evolution of the simulated PM10 was consistent with observations despite relatively high concentrations. The simulated PM2.5 concentrations in Changji and Shihezi were notably lower than those observed, resulting in a lower AQI. For PM10, the simulation–observation error was relatively small; however, the trends were inconsistent. Future research should focus on optimizing model parameterization schemes and emission source data.

Keywords: dust; air pollution; WRF-CUACE; evaluation

1. Introduction

Aerosols play a crucial role in the atmosphere as they impact the radiation balance through the absorption and scattering of shortwave and longwave radiation [1,2]. This both directly and indirectly affects various aspects, such as global surface temperature, climate patterns, hydrologic cycles, and terrestrial ecosystems [3]. Dust aerosols account for approximately 25% of the global total aerosol mass and possess strong absorption properties that directly affect the radiative balance and thermal equilibrium of the Earth–atmosphere system, accelerating the melting rate of surface snow [4,5]. Furthermore, dust aerosols

transport elements such as nitrogen and iron over long distances to the oceans, leading to eutrophication and consequently affecting the global carbon cycle [6]. However, dust aerosols can adversely affect human health and increase the risk of respiratory and cardiovascular diseases [7,8].

Moreover, dust storms can reduce the lifespan of electrical equipment, impact urban transportation, lower solar energy efficiency, and damage crop yields [9–11]. Xinjiang Province is a typical arid and semi-arid area in China characterized by a dry climate, scarce precipitation, sparse vegetation, and strong winds, making the surface susceptible to wind erosion and dust emissions. Frequent dust activity poses a significant threat to the ecological environment in arid regions [12]. Dust events are particularly prevalent during the warm season in the Taklamakan Desert with high concentrations noticeably impacting the surrounding areas [13]. Bao et al. [14] analyzed dust events from 2016 to 2020 using high-resolution imagery from the Himawari-8 satellite and found that the Taklamakan Desert experienced 138 dust events, which was the highest frequency of dust occurrences in East Asia.

Ensuring good air quality is crucial for maintaining healthy living environments. Long-term exposure to polluted air deteriorates the respiratory system and increases the risk of cardiovascular diseases [15,16]. In recent years, China has placed a strong emphasis on promoting high-quality economic growth by implementing environmentally friendly measures aimed at decreasing pollution and carbon emissions as well as safeguarding the ecological environment. Therefore, the precise prediction of air quality is vital for protecting public health and shaping governmental strategies for pollution prevention and control. The economic center of Xinjiang is situated north of the Tianshan Mountains and is heavily reliant on heavy industries with a high concentration of industrial factories. Over the past decade, this area has contributed over 50% of Xinjiang's GDP [17]. However, this area faces challenges related to high pollution levels, particularly during the winter months, when emissions from coal and biomass burning increase. These emissions, combined with unfavorable meteorological conditions that hinder pollutant dispersion, have led to significant increases in atmospheric pollutant levels. It is widely recognized that human activities, such as industrial processes, are the primary sources of air pollution in this region [18–22].

Given these circumstances, accurate prediction and early warning provisions for dust and air pollution events are essential for the advancement, growth, and welfare of the population of Xinjiang. To address the need for accurately forecasting dust storms and severe pollution events, a dust–air pollution forecasting system was developed based on the Weather Research and Forecasting model coupled with the China Meteorological Administration Unified Atmospheric Chemistry Environment (WRF-CUACE) model [23], which was designed to meet the unique dust and environmental prediction requirements of Xinjiang. Regional models have advantages in forecasting dust and air pollution events due to their high spatial resolution, which enables a better simulation of meteorological elements such as temperature, humidity, and wind speed [24]. The WRF-CUACE model, based on the WRF-Chem model (version 3.8.1), effectively simulates meteorological conditions as well as the emissions, formation, transport, mixing, chemical reactions, deposition, and radiative effects of trace gases and aerosols. Therefore, it has unique advantages in simulating dust storms and atmospheric pollution [25–27]. The WRF-CUACE model can accurately simulate the basic characteristics of dust and pollution processes and is widely used in their simulation and forecasting [13,23,28–31]. However, owing to differences in model parameterization schemes, meteorological conditions, and surface characteristics, the simulation results exhibit a level of uncertainty with significant variations between regions [32,33].

This study aimed to evaluate a dust–air pollution forecasting system based on the WRF-CUACE model. The remainder of this paper is organized as follows: Section 2 describes the observational data, WRF-CUACE model domain, physics schemes, and evaluation methodology. Section 3 evaluates the simulation results for dust and air pollution events

using both ground- and satellite-based measurements. Section 4 presents the principal conclusions and recommendations for future research.

2. Data and Methods

2.1. Study Region

Xinjiang, China, is situated in the western part of the Central Asian region. The world's second largest shifting desert, the Taklamakan Desert, is located in the southern Xinjiang on the southside of the Tienshan Mountains (Figure 1). During spring and summer, the occurrence of dust storms in the Taklamakan Desert and neighboring regions of southern Xinjiang noticeably impacts agriculture, transportation, tourism, and the production of solar and wind energy. Conversely, during autumn and winter, major industrial cities in northern Xinjiang often experience air pollution events that present health hazards to the local population. To enhance predictive capabilities for dust and air pollution events and minimize their consequences, we developed a dust–air pollution forecasting product based on the WRF-CUACE model specifically for Xinjiang. The model is activated every day at 08:00 Beijing Standard Time using a 9 km resolution for the entire region and a 3 km resolution for pollution-concentrated cities in northern Xinjiang. It provides hourly forecasts for the next 156 h, including spatial distribution and monitoring station forecasts for PM2.5, PM10, NO_2, SO_2, CO, O_3, the Air Quality Index (AQI), and dust intensity. Furthermore, it provides balloon trajectory forecasts for Ürümqi, Changji, and Shihezi.
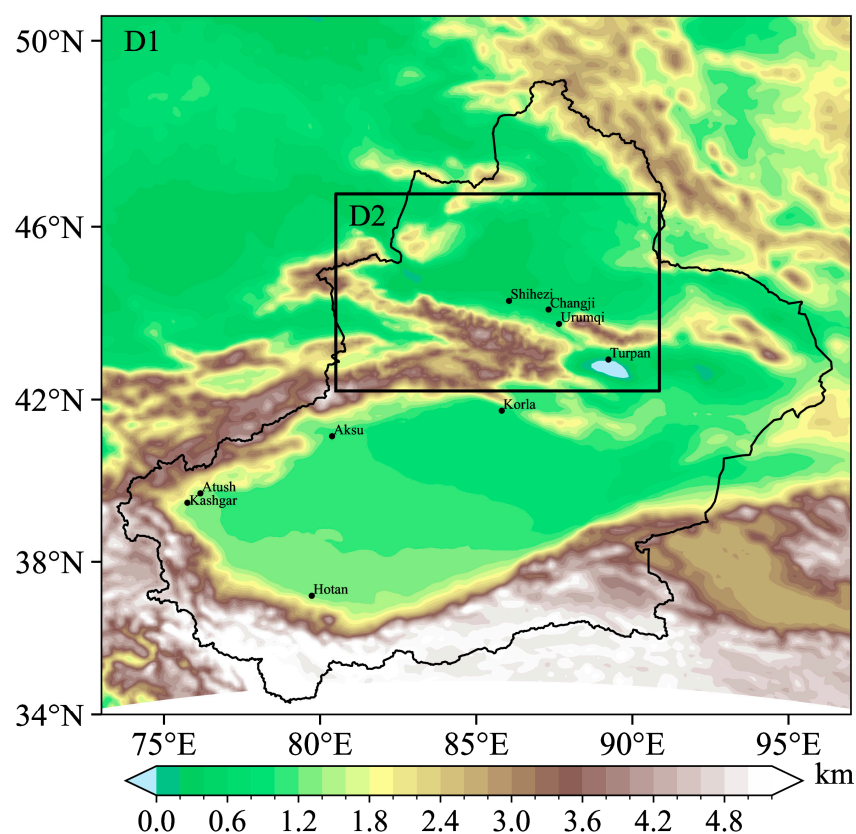

Figure 1. Domains and terrain height of the WRF-CUACE model. Black dots denote the location of environmental monitoring stations.

2.2. Observational Data

In this study, ground and satellite observations are used to validate the model's performance only. The hourly surface 2 m temperature and 10 m wind speed data were obtained from the China Meteorological Administration (http://data.cma.cn/, accessed on 12 January 2023), using national benchmark station. The hourly PM10 and PM2.5 data were obtained from the China National Environmental Monitoring Center (http://www.cnemc.cn/,

accessed on 12 January 2023), using national urban monitoring station. The distribution of the monitoring stations is shown in Figure 1. Daily aerosol optical depth (AOD) remote sensing data were obtained from the Multi-Angle Implementation of Atmospheric Correction (MAIAC) algorithm-based Level-2 gridded aerosol optical thickness product of the MODIS Terra and Aqua satellite combination with a horizontal resolution of 1 km (https://ladsweb.modaps.eosdis.nasa.gov/missions-and-measurements/products/MCD19A2, accessed on 12 January 2023). MAIAC is a new advanced algorithm which uses time series analysis and a combination of pixel- and image-based processing to improve accuracy of cloud detection, aerosol retrievals, and atmospheric correction. The AOD is originally retrieved in MODIS blue band B3 (0.47 um). Because the common input for the chemical transport models as well as AOD validation and AOD product intercomparison are standardized to 0.55 um, a "green" band (B4) AOD is also provided. The high spatial resolution AOD data from MAIAC are promising for studying fine aerosols in arid areas and improving local air quality research [34].

2.3. Model Settings

The WRF-CUACE model in the forecasting system used two domains: the outer domain covering the Central Asian region centered on Xinjiang and the inner domain focusing on the primary polluted cities in northern Xinjiang (Figure 1). The horizontal grid dimensions and resolutions were 279×219 (9 km) and 264×165 (3 km), respectively. The vertical direction comprised 32 unevenly spaced sigma layers with a top pressure of 100 hPa. Table 1 lists the physical and chemical parameterization schemes used in the model. The terrain and land use/land cover data incorporated the latest terrain data from the WRF model and MODIS_30s land use data provided by the National Centers for Environmental Prediction, accurately reflecting the complex surface conditions of Xinjiang. The initial fields and boundary conditions, updated every 6 h, were derived from the CMA-GFS (China Meteorological Administration Global Assimilation Forecasting System) data with a resolution of $0.25° \times 0.25°$ (25 km $\times$ 25 km). Anthropogenic emissions are derived from the MIX emission inventory representative for 2010 (http://www.meicmodel.org/dataset-mix.html, accessed on 10 January 2023). The inventory provides monthly grid emission data with $0.25°$ spatial resolution for five emission sectors (electricity, industry, civil, transportation, and agriculture), including PM2.5, PM10, NOx, SO_2, CO, NH_3, black carbon (BC), organic carbon (OC), and non-methane volatile organic compounds (NMVOCs). During the simulation span from 2013 to 2017, China carried out strict air pollution control measures, which had a considerable impact on anthropogenic emissions. To make the anthropogenic emissions more suitable for the real emissions scenarios in the simulated years, the emissions in mainland China were replaced with the MEIC (Multi-resolution Emission Inventory model for Climate and air pollution research) emissions inventory representative for 2012, 2014, and 2016 to represent the emissions scenarios in 2013, 2015, and 2017, respectively [35]. The dust sources are a new dataset of erodibility developed by Li et al. [36] for the GOCART dust emission model, offering a more accurate description of the erosive characteristics of dust source regions. The land cover, vegetation cover vegetation fraction, soil moisture and soil texture data are preprocessed by resampling the resolution (1000 m) and spatial matching by GIS tools. The surface cover map is used to calculate the wind erosion distribution map, where the barren or sparse vegetated land is set to 1 and other areas were 0, to obtain preliminary bare soil surface EROD1 data. The vegetation-free areas are then screened using vegetation coverage, and the vegetation at the pixel scale is removed by multiplying with EROD1 to obtain EROD2. Based on this step, soil texture data are introduced to determine areas with a sand content ratio greater than 0.6 as potential sand source areas to obtain EROD3. Subsequently, SMAP soil moisture data were used to identify regions with soil moisture) less than 0.1, obtaining a surface prone to wind erosion, EROD4.

Table 1. Parameterization schemes of the WRF-CUACE model.

Physics Schemes	Options
Shortwave radiation	RRTMG
Longwave radiation	RRTMG
Microphysics	Lin
Cumulus	New Grell
Planet boundary layer	YSU
Surface layer	Revised MM5
Land surface	Noah
Chemical process	RADM2 and GOCART
Aerosol chemistry	GOCART
Dust emission	Simple GOCART

RRTMG: Rapid Radiative Transfer Model for General Circulation Models. Lin: Lin Microphysics Scheme. YSU: Yonsei University Planetary Boundary Layer Scheme. RADM2: Regional Acid Deposition Model version 2. GOCART: Global Ozone Chemistry Aerosol Radiation and Transport Model.

Dust size distribution in the GOCART module is approximated by five dust bins [37]. Dust density is assumed to be 2500 kg·m^{-3} for the first dust bin and 2650 kg·m^{-3} for dust bins 2–5. The GOCART module calculates the vertical dust flux in five-size bins based on the 10 m wind speed, soil erodibility factor, and other constant parameters. The dust emission mass flux *Fp* for each size bin is determined using Equation (1):

$$Fp = \begin{cases} CSs_p u_{10m}^2(u_{10m} - u_t), & u_{10m} > u_t \\ 0, & u_{10m} \leq u_t \end{cases} \tag{1}$$

where *C* is a spatially uniform factor which controls the magnitude of dust emission flux; *S* is the source function that characterizes the spatial distribution of dust emissions; s_p is the fraction of each size class of the emitted dust bins (p = 1, 2, …, 5); u_{10m} is the horizontal wind speed at 10 m; and u_t is the threshold velocity, which is a function of dust particle density and size, and it is determined by using Equation (2):

$$u_t = 0.13\left(\frac{\rho_d g d}{\rho_a}\right)^{0.5}\left(\frac{\left(1 + \frac{0.06}{\rho_d g d^{2.5}}\right)}{1.928(1.331 d^{1.56} + 0.38)^{0.92} - 1}\right) \tag{2}$$

where ρ_d is the density of the dust particles; ρ_a is the density of dry air; d is the particle diameter, and g is the acceleration due to gravity.

2.4. Model Data Processing

Studies have shown a correlation between the atmospheric dust concentrations in desert regions and elevated AOD [38]. Therefore, the performance of the model for predicting the horizontal distribution of dust events was evaluated using the MODIS AOD dataset. The simulated AOD was calculated using Equations (3) and (4):

$$z = \frac{ph + phb}{9.8 \times 1000} \tag{3}$$

$$\text{AOD} = \int_0^Z extcof55 dz \tag{4}$$

where z denotes the model layer height; *ph* is the perturbation geopotential height; *phb* is the base geopotential height, and *extcof55* is the atmospheric extinction coefficient at 550 nm. *ph*, *phb*, and *extcof55* are variables output directly by the model.

In order to compare the spatial distribution of AOD between MODIS and WRF-CUACE, we performed spatial correlation on the two datasets. Since the spatial resolution of MODIS AOD is 1 km, higher than WRF-CUACE, we resampled the MODIS AOD according to the WRF-CUACE grids with NaN values not included in the statistics.

2.5. Evaluation Metrics

To evaluate the performance of the model in forecasting dust and air pollution events, we used statistical metrics including the correlation coefficient (R), mean absolute error (MAE), and root mean square error (RMSE). The formulas are presented in Equations (5)–(7):

$$R = \frac{\sum_{i=1}^{N} \left(F_i - \overline{F}\right)\left(O_i - \overline{O}\right)}{\sqrt{\sum_{i=1}^{N} \left(F_i - \overline{F}\right)^2 \sum_{i=1}^{N} \left(O_i - \overline{O}\right)^2}} \tag{5}$$

$$MAE = \frac{1}{N}\sum_{i=1}^{N}\left(|F_i - O_i|\right) \tag{6}$$

$$RMSE = \sqrt{\frac{\sum_{i=1}^{N}(F_i - O_i)^2}{N}} \tag{7}$$

where F_i and O_i represent the simulated and observed values for the ith sample, respectively, and $\overline{F}$ and $\overline{O}$ are their mean values, respectively. The correlation coefficient (R) reflects the consistency in trends between the simulated and observed values. The MAE represents the average deviation between the simulated and observed values. The RMSE quantifies the overall deviation between the simulated and observed values. Instances with missing observational data were excluded from these calculations, ensuring the overall results remained unaffected.

3. Results

3.1. Assessment of Dust Process

Meteorological conditions play crucial roles in the formation and development of dust storms. Therefore, observational data from meteorological stations were used to assess the forecasting performance of the model for the meteorological parameters. As illustrated in Figure 2, the model accurately predicted 2 m temperature data, which closely aligned with the observed trends at all six stations. The simulated and observed 2 m temperature data exhibited a high correlation with an R-value of 0.94 at Korla station. The model predictions showed a relatively small bias compared to that of observations with MAE values ranging from 1.61 to 2.39 °C and RMSE values ranging from 1.94 to 3.25 °C (Table 2). Notably, the model tended to underestimate the minimum nighttime temperature (Figure 2). In terms of wind speed, the model accurately predicted high wind speeds during dust storms (Figure 3) with predicted values closely matching observed values, demonstrating the highest R-value of 0.63 at Korla station. However, there were variations in MAE for wind speed across stations with the smallest MAE of 1.31 m·s^{-1} at Turpan station and the largest of 2.21 m·s^{-1} at Hotan station, where the model significantly overestimated the wind speed. The RMSE values at the six stations ranged from 1.65 to 2.69 m·s^{-1} (Table 2), indicating that the forecasting errors of the model are generally within an acceptable range.

Table 2. Correlation coefficient (R), mean absolute error (MAE), and root mean square error (RMSE) between simulations and observations for T2, WS10, and PM10.

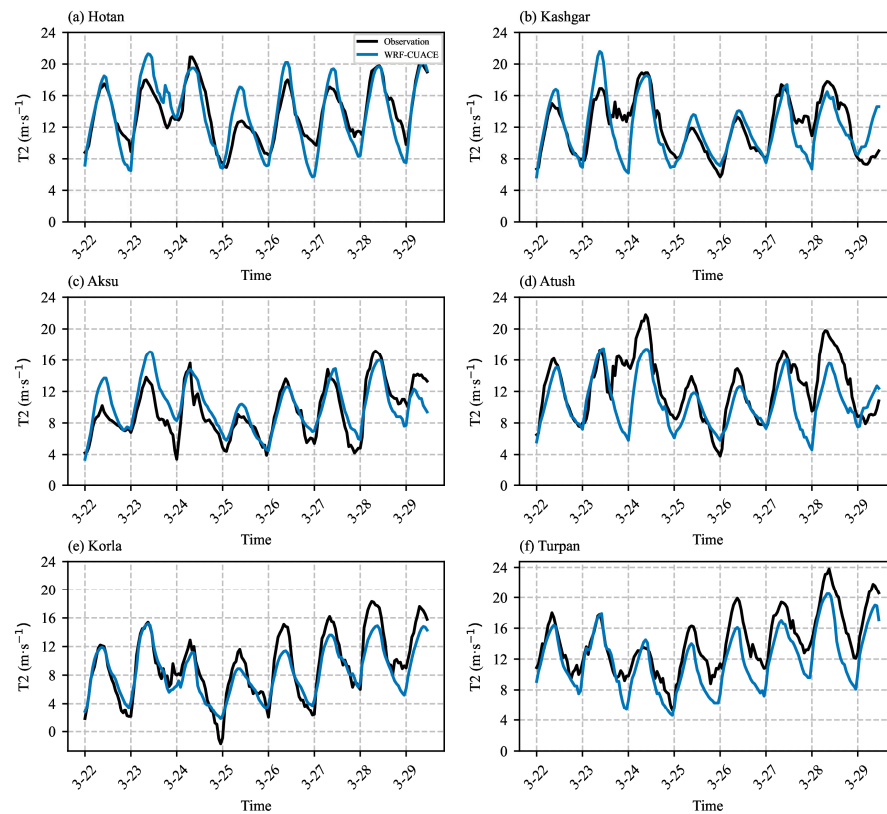| Variables	Indicates	Hotan	Kashgar	Aksu	Atux	Korla	Turpan
	R	0.88	0.76	0.82	0.73	0.94	0.91
T2	MAE	1.61	1.81	1.65	2.45	1.57	2.39
	RMSE	2.06	2.40	2.02	3.25	1.94	2.80
	R	0.34	0.35	0.31	0.51	0.63	0.20
WS10	MAE	2.11	1.43	1.31	1.61	1.82	1.19
	RMSE	2.69	2.03	1.65	2.13	2.35	1.53
	R	0.85	0.54	0.62	0.19	0.43	0.26
PM10	MAE	721.36	840.31	628.65	908.59	599.72	534.11
	RMSE	886.68	1146.70	985.50	1265.40	769.66	650.71

Figure 2. Comparison between simulated and observed 2 m temperature data at (**a**) Hotan, (**b**) Kashgar, (**c**) Aksu, (**d**) Atush, (**e**) Korla, and (**f**) Turpan stations.
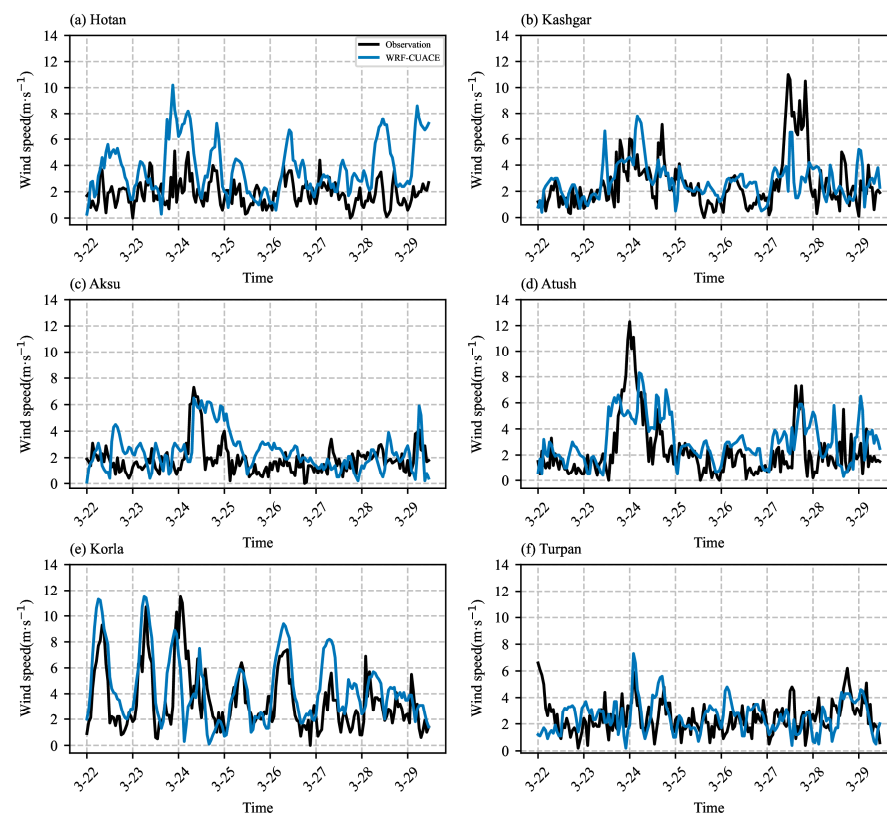

Figure 3. Comparison between simulated and observed 10 m wind speed data at (**a**) Hotan, (**b**) Kashgar, (**c**) Aksu, (**d**) Atush, (**e**) Korla, and (**f**) Turpan stations.

PM10 concentration is a crucial indicator of dust storms with concentrations typically increasing during dust events. To evaluate the dust forecasting performance of the model, the simulated PM10 data were compared with observations from multiple stations during a dust storm (Figure 4), which was followed by a quantitative evaluation (Table 2). The results revealed good agreement between the simulated and observed PM10 concentrations, particularly at the Hotan station, where the model accurately forecasted the peak PM10 concentration on March 25 (Figure 4a), achieving an R-value of 0.85 and an MAE of 721.36 $\mu g \cdot m^{-3}$. This demonstrated the proficiency of the model in predicting severe dust events. The model also exhibited satisfactory performance in predicting peak values at the Aksu and Korla stations (Figure 4c,e), with R-values of 0.6 and 0.43, respectively, albeit with slightly higher MAE values. Although the predicted peaks at Kashgar, Atux, and Turpan stations lagged behind the observations (Figure 4b,d,f), the model adequately captured the overall trend in dust concentration variations. The RMSE values for the six stations ranged from 650.71 to 1265.40 $\mu g \cdot m^{-3}$, indicating acceptable performance for severe dust events. Overall, despite the tendency of the model to overestimate dust intensity at different stations to varying degrees, it proficiently predicted the initiation, progression, and termination of dust events, demonstrating strong performance in predicting fluctuations in dust intensity and peak occurrence times.
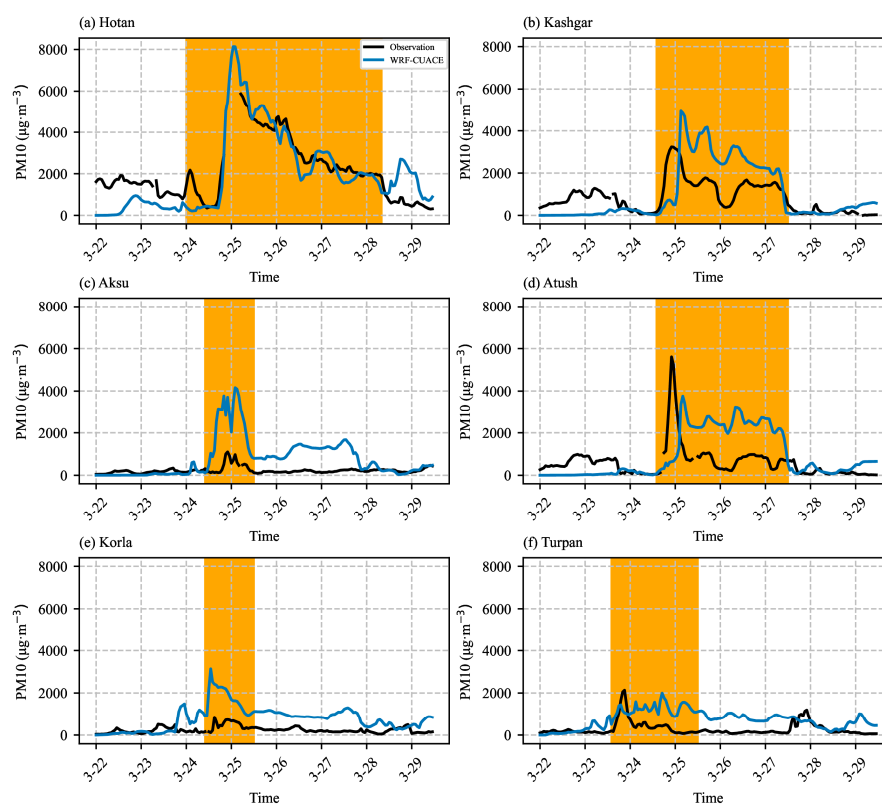

Figure 4. Comparison between modeled and observed particulate matter (PM)10 data at (**a**) Hotan, (**b**) Kashgar, (**c**) Aksu, (**d**) Atushi, (**e**) Korla, and (**f**) Turpan stations.

Figure 5 illustrates the daily averaged distribution of MODIS and simulated AOD from March 24 to 26, indicating a strong agreement in the spatial distribution between the simulated and observed AOD. The model effectively predicted both the spatial distribution and intensity features of AOD in the western Taklamakan Desert in southern Xinjiang. The high AOD values on March 25 and 26 aligned with the high PM10 concentrations observed, especially on March 25, where the spatial correlation reaches 0.78 (Table 3). Nevertheless, the model overestimated AOD intensity in the eastern Xinjiang Basin, as shown in Figure 4f. Despite certain forecasting errors, the model effectively predicted the

spatiotemporal distribution of dust storms, highlighting its capability for dust forecasting and early warnings.
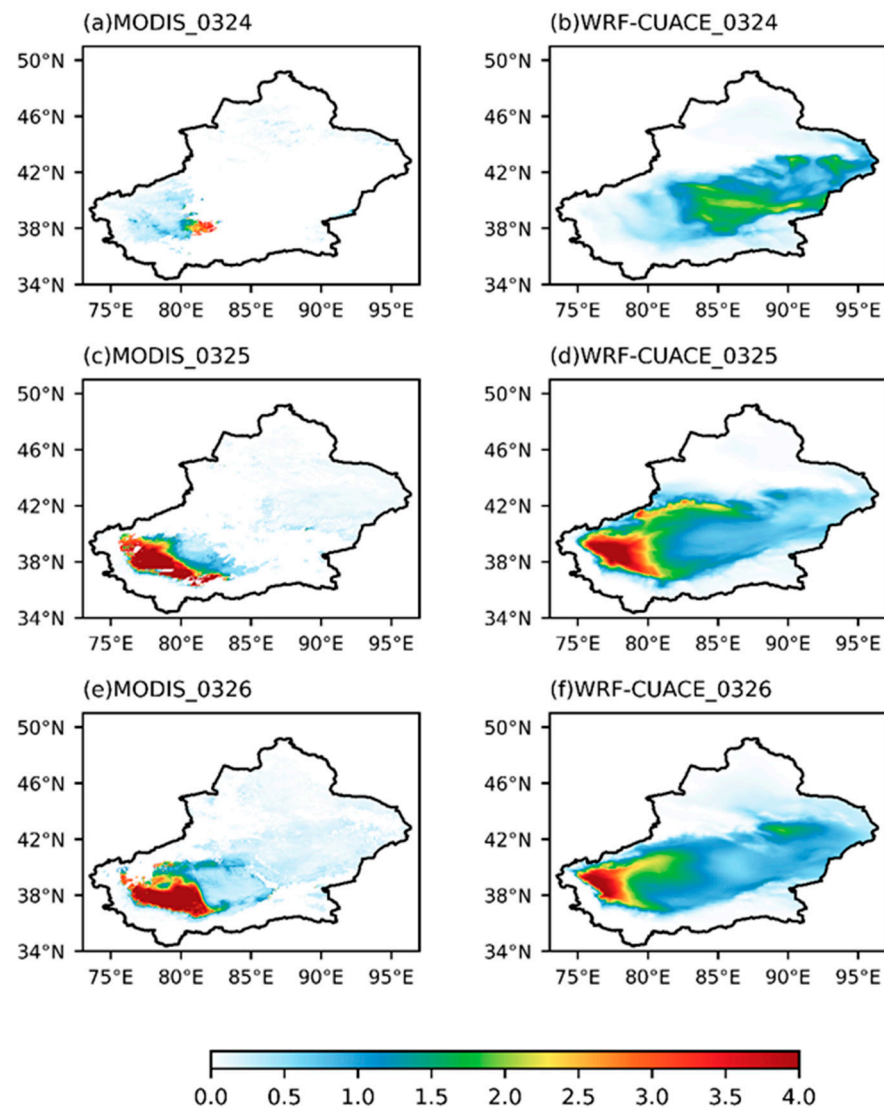

Figure 5. Comparison between simulated aerosol optical depth (AOD) and MODIS satellite observations from 24 to 26 March 2022.

Table 3. Spatial correlation coefficient (R) between simulations and observations for AOD.

Variables	Indicates	March 24	March 25	March 26
AOD	R	0.35	0.78	0.58

3.2. Analysis of Dust Process

Figure 6 presents the spatial distribution of the daily averaged dust emission flux, dust transport flux, and dust deposition flux from 24 to 25 March 2022, to characterize the details of the dust process. On March 24, dust emission occurred in eastern Xinjiang and the northeastern Taklamakan Desert, where Gobi and the desert terrain experienced high wind speeds greater than 6 m·s^{-1}, leading to dust emission under strong wind erosion (Figure 6a). However, on March 25, the wind speed zone moved westward and decreased, resulting in a shift in the dust emission area to the eastern and southern regions of the Taklamakan Desert with a significant decrease in intensity compared to that on March 24 (Figure 6b).
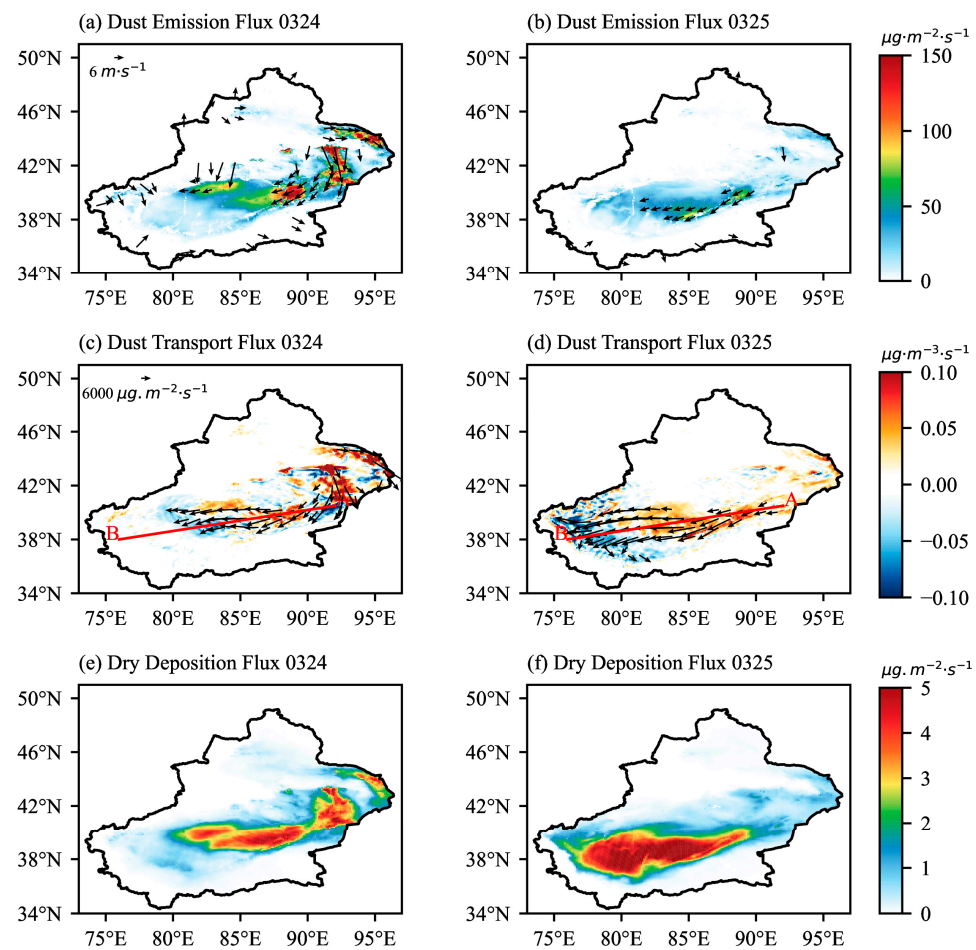
Figure 6. Spatial distribution of averaged dust emission fluxes coupled with 10 m wind speed (**a**,**b**), dust transport fluxes and divergence (**c**,**d**), and dry dust deposition fluxes (**e**,**f**) from 24 to 25 March 2022.

Figure 6c,d illustrate the transport and divergence of dust aerosols by low-level flows in three primary directions on March 24. The dust transmission flux is obtained by multiplying the average wind speed and the average dust concentration below 2500 m. The sources of transportation were consistent with the areas of dust emission. One direction led eastward to northern China, whereas the other two directions led southward and westward to the eastern and central Taklamakan Desert, respectively. On March 25, the transport of dust aerosols continued with accumulation occurring in the western Taklamakan Desert and cities in western Xinjiang (Figure 6e,f).

Vertical profiles were constructed along line AB from 08:00 on March 24 to 00:00 on March 26 to illustrate the vertical structure of the dust event. Line AB (Figure 6c,d), located 1000 m above sea level (Figure 1), is characterized by relatively flat terrain favorable for easterly winds and dust aerosols. On March 24, easterly winds intruded from altitudes below 2500 m with speeds exceeding 8 m·s^{-1}, leading to the formation of dust storms in the eastern Taklamakan. Dust concentrations exceeded 5000 µg·m^{-3} with dust layers reaching a thickness of up to 200 m. As lower-level wind speeds decreased, the dust storm developed, reaching a dust layer thickness of 1000 m by 16:00 on March 24 before shifting toward the central Taklamakan Desert. Although the vertical development of the dust storm subsided, its intensity remained high, exceeding 5000 µg·m^{-3}, as it continued to progress westward toward the western Taklamakan. The easterly winds significantly weakened as they encountered high mountains, resulting in the accumulation of dust aerosols to the east of the mountains with thicknesses of approximately 1800 m. Eventually, the dust storm traversed the mountains and reached a height of 3500 m (Figure 7). To a certain extent,

the height of dust aerosols matches the height of the boundary layer especially in areas with moderate dust concentration during the day. In areas with higher dust concentration, the boundary layer height is slightly lower than the dust height, suggesting that high dust concentration may affect the development of the boundary layer.
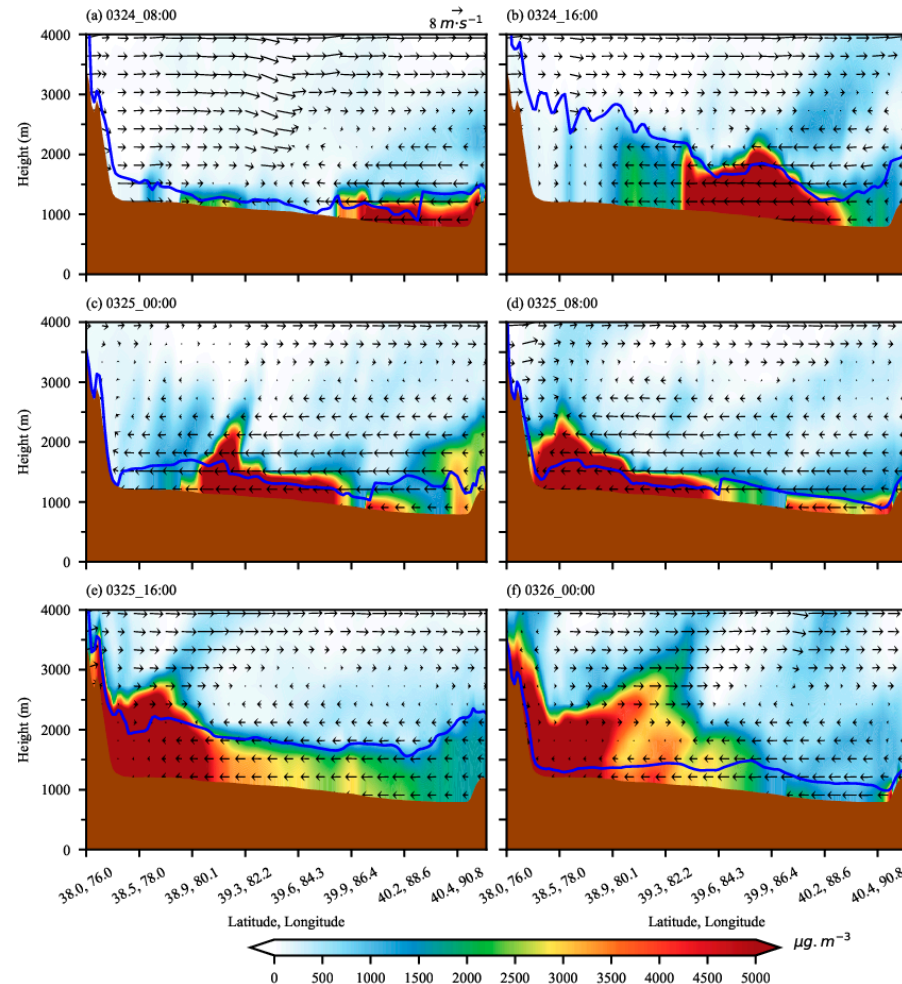

Figure 7. Vertical distribution of averaged dust concentrations and wind vectors along line AB [(92.0°E, 40.5°N) to (76.0°E, 38.0°N)] from 24 to 26 March 2022. Brown field represents terrain height (units: m), and blue lines represents boundary layer height (units: m).

3.3. Assessment of Pollution Process

PM2.5 and PM10 constitute the main sources of pollution in the urban agglomeration situated on the northern slope of the Tianshan Mountains. From 2017 to 2019, the annual average number of days with PM2.5 as the primary pollutant surpassed 90 d in Ürümqi, Changji, and Shihezi. Meanwhile, the average number of days with PM10 as the primary pollutant ranged from 5 to 15 d [22]. Therefore, to assess the prediction performance of the forecasting system, we compared the simulated PM2.5 and PM10 concentration data with the observations from Ürümqi, Changji, and Shihezi during the pollution period from 14 to 26 December 2023 (Figure 8) and conducted quantitative evaluations (Table 4). To present a comprehensive overview of the pollution scenario in these three cities, the observational results from different environmental monitoring stations within the same city were averaged. Similarly, simulation results were collected from the grid points closest to the environmental monitoring stations and subsequently averaged.
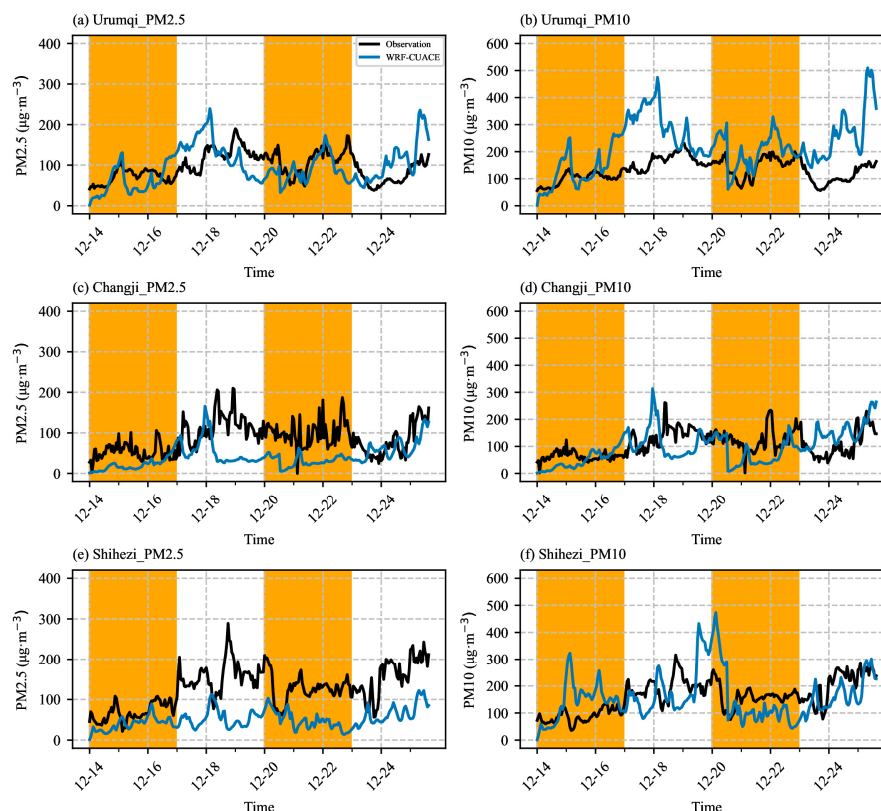
Figure 8. Comparison between simulated and observed PM2.5 and PM10 concentrations in (**a**,**b**) Ürümqi, (**c**,**d**) Changji, and (**e**,**f**) Shihezi from 14 to 26 December 2023.

Table 4. Comparison of R-values, MAE, and RMSE between simulated and observed PM2.5, PM10, and AQI.

Variables	Indicates	Ürümqi				Changji				Shihezi			
		24 h	48 h	72 h	280 h	24 h	48 h	72 h	280 h	24 h	48 h	72 h	280 h
PM2.5	R	0.60	0.54	0.32	0.35	0.51	0.17	0.04	0.18	0.53	0.12	0.27	0.33
	MAE	28.92	29.10	32.32	40.59	55.06	53.31	51.87	52.24	43.03	48.40	54.73	76.78
	RMSE	32.03	33.59	38.69	48.61	57.40	57.72	57.81	63.32	53.06	56.13	61.26	90.02
PM10	R	0.78	0.64	0.62	0.46	0.56	0.01	0.03	0.21	0.76	0.23	0.25	0.27
	MAE	54.15	47.43	56.83	95.58	51.16	52.03	48.46	56.61	67.59	82.08	74.94	73.65
	RMSE	61.57	57.88	71.33	125.10	60.31	62.23	59.73	70.30	83.03	103.72	94.87	92.34
AQI	R	0.79	0.70	0.54	0.39	0.52	0.01	0.05	0.19	0.72	0.24	0.27	0.26
	MAE	24.21	27.56	30.91	47.45	67.62	68.05	64.08	61.22	39.17	56.49	58.67	76.67
	RMSE	28.59	32.15	36.92	63.90	72.81	76.19	73.50	75.67	47.03	66.64	67.29	90.80

Figure 8 presents a comparison between the simulated and observed levels of PM2.5 and PM10, the two primary pollutants, in the three urban areas. The analysis revealed that the accuracy of the model in forecasting these pollutants varied considerably among the cities. Specifically, Ürümqi showed the most accurate PM2.5 estimations, and the model successfully captured the trends in PM2.5 concentrations. The R-values between the simulation and observation for 24 and 48 h intervals were 0.60 and 0.54, respectively, with the simulated peak times aligning closely with those of the actual observations (Figure 8a). Moreover, the errors between simulations and observations were relatively small, with 24 and 48 h MAEs of 28.92 and 29.10 $\mu g \cdot m^{-3}$, respectively, and an MAE of 40.59 $\mu g \cdot m^{-3}$ for 280 h intervals. In contrast, the PM2.5 forecasting performance in Changji and Shihezi was notably inferior to that in Ürümqi. Between December 18 and 24, the model failed to accurately predict high PM2.5 concentrations with the simulated concentrations being lower than the observations (Figure 8c,e). Although the R for 24 h intervals exceeded 0.5,

the MAE and RMSE were relatively large, indicating significant discrepancies between the model forecasts and observations.

For PM10 simulation, the model accurately predicted the trend in PM10 variations in Ürümqi, with R-values reaching 0.78, 0.64, and 0.72 for 24, 48, and 72 h intervals, respectively. However, the model significantly overestimated PM10 concentrations, resulting in notable errors. The mean MAE and RMSE for 24 h were 54.15 $\mu g \cdot m^{-3}$ and 61.57 $\mu g \cdot m^{-3}$, respectively, while the overall MAE and RMSE for 280 h intervals exceeded 95 $\mu g \cdot m^{-3}$. In comparison, the PM10 forecasting errors in Changji were relatively minor and stable with MAE differences within 5 $\mu g \cdot m^{-3}$ and RMSE differences within 10 $\mu g \cdot m^{-3}$ across various forecast lead times. However, there were significant differences in the R-values for different forecast lead times in Changji, indicating poor forecasting trends. In Shihezi, the R for 24 h intervals reached 0.76, with an MAE and RMSE of 67.59 $\mu g \cdot m^{-3}$ and 83.03 $\mu g \cdot m^{-3}$, respectively. Conversely, the R-values for other forecast lead times were lower, and the MAE and RMSE were larger, indicating significant forecasting errors.

The AQI is a crucial indicator for quantitatively assessing air quality, directly reflecting its impact on human health. This forecast quantity has received considerable attention in daily life. The formula for the AQI model follows the Industry Standard of Air Quality Forecasting in China, as shown in Equations (8) and (9):

$$\text{IAQI}_\text{p} = \frac{(C_P - C_{BP,Lo})\,(IAQI_{Hi} - IAQI_{Lo})}{C_{BP,Hi} - C_{BP,Lo}} + IAQI_{Lo} \tag{8}$$

$$\text{AQI} = max\left\{ IAQI_{pm2.5}, IAQI_{pm10}, IAQI_{no2}, IAQI_{so2}, IAQI_{co}, IAQI_{o3} \right\} \tag{9}$$

where $IAQI_P$ represents the air quality sub-index of pollutant P (PM2.5, PM10, NO$_2$, SO$_2$, CO, and O$_3$); C_p denotes the mass concentration of pollutant P; $C_{PB,Lo}$ and $C_{PB,Hi}$ are the lower and upper limits of pollutant concentration values closely related to C_p, respectively; $IAQI_{Lo}$ corresponds to $C_{PB,Lo}$ and represents the air quality sub-index; and $IAQI_{Hi}$ corresponds to $C_{PB,Hi}$ and represents the air quality sub-index.

Figure 9 compares the simulated and observed AQI values. Significant disparities in the predictive performance of the AQI were evident across different cities. The model exhibited the most favorable predictive performance in Ürümqi, accurately tracking AQI trends with predicted peaks that closely matched the observed values (Figure 9a). The R-values for the 24 and 48 h intervals were 0.79 and 0.70, respectively. Moreover, the prediction errors were relatively minor, with MAEs of 24.21 and 27.56 for the 24 and 48 h intervals, respectively. Even for 280 h intervals, the MAE was 47.45, which is below the minimum cutoff for the AQI classification. In contrast, the model yielded reasonably accurate predictions for the first 24 h intervals in Changji and Shihezi, with R-values of 0.52 and 0.72, respectively. However, after the first 24 h, the R-values decreased to less than 0.3 with an MAE exceeding 50. The model failed to accurately capture the observed peak values and significantly underestimated the AQI (Figure 9b,c).
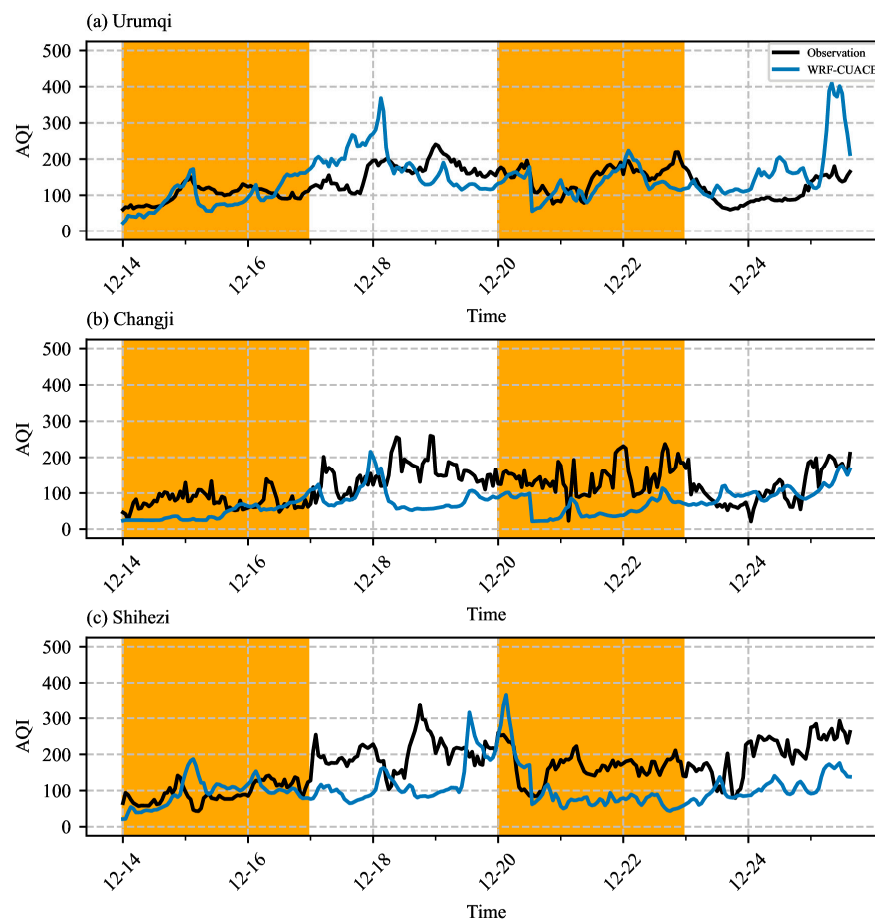
Figure 9. Comparison between simulated and observed AQIs in (**a**) Ürümqi, (**b**) Changji, and (**c**) Shihezi from 14 to 26 December 2023.

4. Discussion

Overall, this study preliminarily evaluated the accuracy and reliability of a dust and air pollution forecasting system based on the WRF-CUACE model. The results highlighted that the model generally provides accurate forecasts of meteorological conditions during dust events particularly for predicting temperature and wind speed. The wind speed predictions closely matched the observations, particularly for capturing peak wind speeds, which are crucial for simulating dust movement. The predicted PM10 concentrations showed a trend consistent with the observations particularly at the time of the dust peak. This study also showed that the simulated spatial distribution and intensity of AOD were consistent with observations from the MODIS satellite. Another major finding was that the model's prediction performance varied significantly across different cities during the pollution process with high R- and low RMSE values for PM2.5 and AQI at different time intervals in Ürümqi.

In contrast to earlier evaluations conducted by Han et al. [39], we found that the simulated PM10 showed a better match with the observations at Hotan station during the dust storm. The horizontal characteristics of dust emissions and transport also supported the results of recent studies [4,13,28], and we provided the vertical evolution structure of the dust storms to more clearly reveal its characteristics. In addition, the assessment of prediction performance for the primary pollutants in Xinjiang complements the research conducted by Zhang et al. [23], who developed a WRF-CUACE model and evaluated its performance in simulating air quality in eastern China.

However, this study had certain limitations. There were instances of wind speed and dust intensity overestimations in the forecasts, and the PM10 level in Ürümqi was higher than expected, while the PM2.5 levels in Changji and Shihezi were significantly

lower during the air pollution events. These results may be attributed to the parameter configurations of the model and additional influencing factors, such as surface conditions, dust, and anthropogenic emissions. Because of the spatiotemporal resolution and representative scenarios, the quality of anthropogenic emissions inventory may be the major influencing factor causing uncertainty. Additionally, this study evaluated only two typical events. Future studies should focus on enhancing the performance of this model. Adjustments are required in the parameterization scheme to mitigate wind speed overestimation and dust intensity forecasting errors. Furthermore, the optimization of the simulation parameters and input data tailored to specific city conditions is essential for enhancing the forecasting accuracy of PM2.5 and PM10 in Changji and Shihezi. Future research should include a comprehensive evaluation of dust and pollution events at different temporal and spatial scales.

5. Conclusions

Air pollution has become a significant issue that threatens human health and environmental resources [40].This study used ground and satellite observational data to evaluate dust and air pollution forecasting systems based on the WRF-CUACE model. Preliminary forecasting performance results were obtained at different temporal and spatial scales during a dust and air pollution event. The conclusions are as follows:

(1) During the dust event, the model performed well in predicting meteorological conditions. The 2 m temperature data exhibited a high correlation across all stations, especially in the Turpan area, where the R-value reached 0.94. The errors were reasonable with the MAEs of the six stations ranging from 1.61 to 2.45 °C. The wind speed R-values were between 0.20 and 0.61, and the RMSEs were below 2.61 $m \cdot s^{-1}$.

(2) The WRF-CUACE model accurately predicted the timing of the dust peak, and the PM10 trend was consistent with observations. The Hotan station yielded the highest R-value (0.85) with MAE and RMSE values of 721.36 and 886.68 $\mu g \cdot m^{-3}$, respectively. For the Aksu, Kashgar, and Korla stations, the R-value exceeded 0.4 with MAE values ranging from 599.72 to 840.31 $\mu g \cdot m^{-3}$. However, the Atux and Turpan regions demonstrated relatively low correlation coefficients. Additionally, the model demonstrated good capability for predicting the AOD with the spatial R of 0.78 at March 25.

(3) Dust emissions occurred in eastern Xinjiang and the northeastern Taklamakan Desert. Under the influence of strong easterly wind, with speeds greater than 8 $m \cdot s^{-1}$ and a dust layer thickness of 2000 m, dust storms occurred and propagated westward. The intensity of the dust storms exceeded 5000 $\mu g \cdot m^{-3}$ with a thickness reaching 1800 m. Due to the blocking effect of the high mountains in western Xinjiang, wind speeds decreased, and dust particles accumulated and descended over the cities in western Xinjiang.

(4) During the air pollution event, significant differences were observed in the forecasting performance for PM2.5 and PM10 across different cities. Ürümqi exhibited the best performance, whereas Changji and Shihezi exhibited relatively poor results. The AQI forecast of the model performed well in Ürümqi with R-values greater than 0.7 for both 24 and 48 h intervals and MAEs less than 30 $\mu g \cdot m^{-3}$. Conversely, significant forecasting errors were observed for Changji and Shihezi.

Author Contributions: Conceptualization, A.M.; data curation, A.M. and Y.W.; funding acquisition, A.M.; methodology, Y.W. and H.L. (Huoqing Li); writing—original draft, Y.W.; writing—review and editing, Y.W.; software, Y.W. and L.Z.; validation, A.M., J.L., W.H., H.L. (Hongli Liu) and L.Z.; formal analysis, H.L. (Huoqing Li); investigation, Y.W.; data curation, Y.W.; writing—original draft preparation, Y.W.; writing—review and editing, Y.W.; visualization, Y.W.; supervision, A.M.; project administration, L.Z.; funding acquisition, A.M. All authors have read and agreed to the published version of the manuscript.

References

1. Sokolik, I.N.; Winker, D.; Bergametti, G.; Gillette, D.; Carmichael, G.; Kaufman, Y.; Gomes, L.; Schuetz, L.; Penner, J. Introduction to special section: Outstanding problems in quantifying the radiative impacts of mineral dust. *J. Geophys. Res. Atmos.* **2001**, *106*, 18015–18027. [CrossRef]
2. Heinold, B.; Tegen, I.; Schepanski, K.; Hellmuth, O. Dust radiative feedback on Saharan boundary layer dynamics and dust mobilization. *Geophys. Res. Lett.* **2008**, *35*, L20817. [CrossRef]
3. Rizza, U.; Avolio, E.; Morichetti, M.; Di Liberto, L.; Bellini, A.; Barnaba, F.; Virgili, S.; Passerini, G.; Mancinelli, E. On the Interplay between Desert Dust and Meteorology Based on WRF-Chem Simulations and Remote Sensing Observations in the Mediterranean Basin. *Remote Sens.* **2023**, *15*, 435. [CrossRef]
4. Liu, J.; Ding, J.; Rexiding, M.; Li, X.; Zhang, J.; Ran, S.; Bao, Q.; Ge, X. Characteristics of dust aerosols and identification of dust sources in Xinjiang, China. *Atmos. Environ.* **2021**, *262*, 118651. [CrossRef]
5. Sreekanth, V. Dust aerosol height estimation: A synergetic approach using passive remote sensing and modelling. *Atmos. Environ.* **2014**, *90*, 16–22. [CrossRef]
6. Guo, J.; Lou, M.; Miao, Y.; Wang, Y.; Zeng, Z.; Liu, H.; He, J.; Xu, H.; Wang, F.; Min, M. Trans-Pacific transport of dust aerosols from East Asia: Insights gained from multiple observations and modeling. *Environ. Pollut.* **2017**, *230*, 1030–1039. [CrossRef] [PubMed]
7. Kanatani, K.T.; Ito, I.; Al-Delaimy, W.K.; Adachi, Y.; Mathews, W.C.; Ramsdell, J.W. Desert dust exposure is associated with increased risk of asthma hospitalization in children. *Am. J. Respir.* **2010**, *182*, 1475–1481. [CrossRef] [PubMed]
8. Xu, W.; Sun, Y.; Wang, Q.; Zhao, J.; Wang, J.; Ge, X.; Xie, C.; Zhou, W.; Du, W.; Li, J. Changes in aerosol chemistry from 2014 to 2016 in winter in Beijing: Insights from high-resolution aerosol mass spectrometry. *J. Geophys. Res. Atmos.* **2019**, *124*, 1132–1147. [CrossRef]
9. Hachicha, A.A.; Al-Sawafta, I.; Said, Z. Impact of dust on the performance of solar photovoltaic (PV) systems under United Arab Emirates weather conditions. *Renew. Energy* **2019**, *141*, 287–297. [CrossRef]
10. Middleton, N.J. Desert dust hazards: A global review. *Aeolian Res.* **2017**, *24*, 53–63. [CrossRef]
11. Weinzierl, B.; Sauer, D.; Minikin, A.; Reitebuch, O.; Dahlkötter, F.; Mayer, B.; Emde, C.; Tegen, I.; Gasteiger, J.; Petzold, A. On the visibility of airborne volcanic ash and mineral dust from the pilot's perspective in flight. *Phys. Chem. Earth Parts A/B/C* **2012**, *45*, 87–102. [CrossRef]
12. Shen, Y.-J.; Shen, Y.; Guo, Y.; Zhang, Y.; Pei, H.; Brenning, A. Review of historical and projected future climatic and hydrological changes in mountainous semiarid Xinjiang (northwestern China), central Asia. *Catena* **2020**, *187*, 104343. [CrossRef]
13. Han, Z.; Ge, J.; Chen, X.; Hu, X.; Yang, X.; Du, J. Dust activities induced by nocturnal low-level jet over the Taklimakan desert from WRF-Chem simulation. *J. Geophys. Res. Atmos.* **2022**, *127*, e2021JD036114. [CrossRef]
14. Bao, C.; Yong, M.; Bueh, C.; Bao, Y.; Jin, E.; Bao, Y.; Purevjav, G. Analyses of the dust storm sources, affected areas, and moving paths in Mongolia and China in early spring. *Remote Sens.* **2022**, *14*, 3661. [CrossRef]
15. Chen, R.; Yin, P.; Meng, X.; Wang, L.; Liu, C.; Niu, Y.; Liu, Y.; Liu, J.; Qi, J.; You, J. Associations between coarse particulate matter air pollution and cause-specific mortality: A nationwide analysis in 272 Chinese cities. *Environ. Health Perspect.* **2019**, *127*, 017008. [CrossRef]
16. Karroum, K.; Lin, Y.; Chiang, Y.-Y.; Ben Maissa, Y.; El Haziti, M.; Sokolov, A.; Delbarre, H. A review of air quality modeling. *Mapan* **2020**, *35*, 287–300. [CrossRef]
17. Luo, Y.; Xu, L.; Li, Z.; Zhou, X.; Zhang, X.; Wang, F.; Peng, J.; Cao, C.; Chen, Z.; Yu, H.; et al. Air pollution in heavy industrial cities along the northern slope of the Tianshan Mountains, Xinjiang: Characteristics, meteorological influence, and sources. *Environ. Sci.* **2023**, *30*, 55092–55111. [CrossRef]
18. Li, M.; Zhang, Z.; Li, S.; Yu, X.; Jv, C. Verification of CUACE air quality forecast in urumqi. *Desert Oasis Meteorol.* **2014**, *8*, 63–68.
19. Shen, Y.; Zhang, L.; Fang, X.; Ji, H.; Li, X.; Zhao, Z. Spatiotemporal patterns of recent PM2.5 concentrations over typical urban agglomerations in China. *Sci. Total Environ.* **2019**, *655*, 13–26. [CrossRef]

20. Wang, W.; Samat, A.; Abuduwaili, J.; Ge, Y. Spatio-temporal variations of satellite-based PM2.5 concentrations and its determinants in Xinjiang, northwest of China. *Int. J. Environ. Res.* **2020**, *17*, 2157. [CrossRef] [PubMed]

21. Rupakheti, D.; Yin, X.; Rupakheti, M.; Zhang, Q.; Li, P.; Rai, M.; Kang, S.J.E.P. Spatio-temporal characteristics of air pollutants over Xinjiang, northwestern China. *Environ. Pollut.* **2021**, *268*, 115907. [CrossRef] [PubMed]

22. Li, S.; Li, X.; Mauren, A.; Zhong, Y.; Wang, H. Characteristics of air pollution and its polluted weather types of urban agglomeration on the north slope of the middle Tianshan Mountains from 2017 to 2019. *Arid. Land Geogr.* **2022**, *45*, 1082–1092.

23. Zhang, L.; Gong, S.; Zhao, T.; Zhou, C.; Wang, Y.; Li, J.; Ji, D.; He, J.; Liu, H.; Gui, K. Development of WRF/CUACE v1. 0 model and its preliminary application in simulating air quality in China. *Geosci. Model Dev.* **2021**, *14*, 703–718. [CrossRef]

24. Kim, K.M.; Kim, S.W.; Choi, M.; Kim, M.; Kim, J.; Shin, I.; Kim, J.; Chung, C.Y.; Yeo, H.; Kim, S.W. Modeling Asian dust storms using WRF-Chem during the DRAGON-Asia Field Campaign in April 2012. *J. Geophys. Res. Atmos.* **2021**, *126*, e2021JD034793. [CrossRef]

25. Grell, G.A.; Peckham, S.E.; Schmitz, R.; McKeen, S.A.; Frost, G.; Skamarock, W.C.; Eder, B. Fully coupled "online" chemistry within the WRF model. *Atmos. Environ.* **2005**, *39*, 6957–6975. [CrossRef]

26. Kumar, R.; Barth, M.C.; Pfister, G.G.; Naja, M.; Brasseur, G.P. WRF-Chem simulations of a typical pre-monsoon dust storm in northern India: Influences on aerosol optical properties and radiation budget. *Atmos. Chem. Phys.* **2014**, *14*, 2431–2446. [CrossRef]

27. Liu, L.; Huang, X.; Ding, A.; Fu, C. Dust-induced radiative feedbacks in north China: A dust storm episode modeling study using WRF-Chem. *Atmos. Environ.* **2016**, *129*, 43–54. [CrossRef]

28. Zhao, J.; Ma, X.; Wu, S.; Sha, T. Dust emission and transport in Northwest China: WRF-Chem simulation and comparisons with multi-sensor observations. *Atmos. Res.* **2020**, *241*, 104978. [CrossRef]

29. Ma, Y.; Jin, Y.; Zhang, M.; Gong, W.; Hong, J.; Jin, S.; Shi, Y.; Zhang, Y.; Liu, B. Aerosol optical properties of haze episodes in eastern China based on remote-sensing observations and WRF-Chem simulations. *Sci. Total Environ.* **2021**, *757*, 143784. [CrossRef]

30. Mancinelli, E.; Avolio, E.; Morichetti, M.; Virgili, S.; Passerini, G.; Chiappini, A.; Grasso, F.; Rizza, U. Exposure Assessment of Ambient PM2.5 Levels during a Sequence of Dust Episodes: A Case Study Coupling the WRF-Chem Model with GIS-Based Postprocessing. *Int. J. Environ. Res. Public Health* **2023**, *20*, 5598. [CrossRef]

31. Chen, Y.; Zhang, Y.; Chen, S.; Yang, B.; Yan, H.; Li, J.; Zhang, C.; Lou, G.; Chen, J.; Lian, L. Impacts of dynamic dust sources coupled with WRF-Chem 3.9.1 on the dust simulation over East Asia. *Geosci. Model Dev. Discuss.* **2023**, *17*, 847–864. [CrossRef]

32. Uno, I.; Wang, Z.; Chiba, M.; Chun, Y.; Gong, S.L.; Hara, Y.; Jung, E.; Lee, S.S.; Liu, M.; Mikami, M. Dust model intercomparison (DMIP) study over Asia: Overview. *J. Geophys. Res. Atmos.* **2006**, *111*, D22207. [CrossRef]

33. Huneeus, N.; Schulz, M.; Balkanski, Y.; Griesfeller, J.; Prospero, J.; Kinne, S.; Bauer, S.; Boucher, O.; Chin, M.; Dentener, F.; et al. Global dust model intercomparison in AeroCom phase I. *Atmos. Chem. Phys.* **2011**, *11*, 7781–7816. [CrossRef]

34. Chen, X.; Ding, J.; Wang, J.; Ge, X.; Zhang, Z.; Zhang, Z.; Zuo, H. Validation of the fine resolution of the MODIS MAIAC aerosol optical depth product over arid areas. *Natl. Remote Sens. Bull.* **2023**, *27*, 406–419. [CrossRef]

35. Li, M.; Zhang, Q.; Kurokawa, J.-i.; Woo, J.-H.; He, K.; Lu, Z.; Ohara, T.; Song, Y.; Streets, D.G.; Carmichael, G.R. MIX: A mosaic Asian anthropogenic emission inventory under the international collaboration framework of the MICS-Asia and HTAP. *Atmos. Chem. Phys.* **2017**, *17*, 935–963. [CrossRef]

36. Li, H.; Wang, C.; Wang, M.; Liu, Z.; Mamtimin, A.; Pan, X. A new dataset of erodibility in dust source for WRF-Chem model based on remote sensing and soil texture-Application and Validation. *Atmos. Environ.* **2023**, *315*, 120156. [CrossRef]

37. Ginoux, P.; Chin, M.; Tegen, I.; Prospero, J.M.; Holben, B.; Dubovik, O.; Lin, S.-J. Sources and distributions of dust aerosols simulated with the GOCART model. *J. Geophys. Res. Atmos.* **2001**, *106*, 20255–20273. [CrossRef]

38. Yu, Y.; Notaro, M.; Liu, Z.; Kalashnikova, O.; Alkolibi, F.; Fadda, E.; Bakhrjy, F. Assessing temporal and spatial variations in atmospheric dust over Saudi Arabia through satellite, radiometric, and station data. *J. Geophys. Res. Atmos.* **2013**, *118*, 13253–13264. [CrossRef]

39. Han, T.; Pan, X.; Wang, X. Evaluating and improving the sand storm numerical simulation performance in Northwestern China using WRF-Chem and remote sensing soil moisture data. *Atmos. Res.* **2021**, *251*, 105411. [CrossRef]

40. Semlali, B.-E.B.; El Amrani, C.; Ortiz, G.; Boubeta-Puig, J.; Garcia-De-Prado, A. SAT-CEP-monitor: An air quality monitoring software architecture combining complex event processing with satellite remote sensing. *Comput. Electr. Eng.* **2021**, *93*, 107257. [CrossRef]